8-19-2011

Fluid Structure and Boundary Slippage in Nanoscale Liquid Films

Nikolai V. Priezjev
Wright State University - Main Campus, nikolai.priezjev@wright.edu

Fluid structure and boundary slippage in nanoscale liquid films

Nikolai V. Priezjev

Department of Mechanical Engineering,

Michigan State University, East Lansing, Michigan 48824

(Dated: August 19, 2011)

Abstract

During the last ten years, there has been enormous interest in understanding transport phenomena in micro and nanofluidic systems and, in particular, in accurate prediction of fluid flows with slip boundary conditions at liquid-solid interfaces. In this chapter, we discuss recent results obtained from molecular dynamics simulations of fluids that consist of monomers or linear polymer chains confined by flat crystalline surfaces. The effects of shear rate and wall lattice orientation on the slip behavior are studied for a number of material parameters of the interface, such as fluid and wall densities, wall-fluid interaction energy, polymer chain length, and wall lattice type. A detailed analysis of the substrate-induced fluid structure and interfacial diffusion of fluid molecules is performed to identify slip flow regimes at low and high shear rates.

I. INTRODUCTION

The study of fluid transport through micro and nanochannels is important for biotechnological applications and energy conversion processes [1]. The precise control and manipulation of fluids in systems with large surface-to-volume ratios, however, require fundamental understanding of flow boundary conditions. Fluid velocity profiles can be significantly modified in the presence of slip at a solid surface. The degree of slip is quantified by the slip length, which is defined as a distance between locations of the real interface and imaginary plane where the extrapolated tangential velocity component vanishes. It was shown by numerous experimental studies that the main factors affecting slippage at the liquid-solid interface include surface roughness [2–4], surface wettability [5–7], fluid structure [7–9], and shear rate [10–12]. The slip length in the micron range is reported for complex flows near superhydrophobic surfaces [13] and flows of high molecular weight polymers [14], while the magnitude of the slip length in the range of a few tens of nanometers is typically measured for flows of water over smooth nonwetting surfaces [15].

In recent years, many molecular dynamics (MD) simulation studies have been performed in order to investigate the influence of structural properties of the interface between monatomic fluids and crystalline walls on the degree of slip [16–31] and references therein. Most notably, it was demonstrated that the slip length is strongly correlated with the intensity of structure induced within the first fluid layer by the periodic surface potential [18]. In general, the slippage is suppressed by the strong wall-fluid attraction and/or due to the formation of commensurate structures between solid wall and adjacent fluid layer. A theoretical estimate of the slip length at low shear rates can be obtained via the Green-Kubo relation between the friction coefficient at the interface and the time integral of the autocorrelation function of the lateral force that acts on the adjacent fluid from the solid wall [21]. In most of the MD studies, the solid walls are modeled as an array of atoms arranged on sites of a periodic lattice. Two types of walls are usually considered, solid and thermal, where the wall atoms are either fixed at the lattice sites or allowed to oscillate under the harmonic potential. It was recently found that the slip length weakly depends on the value of the spring stiffness coefficient for sufficiently strong harmonic bonds [26, 29]. In addition, the slope of the shear rate dependence of the slip length is not significantly affected by stiff springs [26], except at very high shear rates [32].

At the interface between *simple fluids* and atomically smooth, weakly attractive surfaces, the slip length is constant only at relatively low shear rates and it increases nonlinearly at high shear rates, as originally reported by Thompson and Troian [27] and later confirmed by several studies [25, 29, 33, 34]. For sufficiently strong wall-fluid interaction and incommensurate structures of the liquid and solid phases at the interface, the slip length varies almost linearly with shear rate [25, 26]. It should be emphasized, however, that if the slip length at low shear rates is less than about a molecular diameter then the boundary conditions for dense monatomic fluids remain independent of shear rate [18, 26, 27]. Also, it was shown that molecular-scale surface roughness reduces the magnitude of the slip length and the slope of its rate dependence [19, 26, 34–36].

It was recently demonstrated that the effective slip length for flows over anisotropic surfaces with two-component texture of different wettability is largest (smallest) for parallel (perpendicular) orientation of stripes with respect to the mean flow [37]. These conclusions hold when the stripe width is comparable to the molecular diameter [38]. For the transverse orientation of the flow relative to the stripes, the slip is reduced because of the molecular scale corrugation of the composed surface potential, while for the parallel orientation, the fluid molecules are transported along homogeneous stripes with either no-slip or partial slip conditions; and, therefore, the effective slip length is enhanced [38]. More recently, it was observed that the slip length also depends on the crystal lattice plane in contact with the fluid and on the lattice orientation with respect to the flow direction [39]. In this chapter, we will show that at sufficiently high shear rates, the slip flow is anisotropic for atomically flat crystalline surfaces; and, in particular, the slip length is enhanced when the shear flow is oriented along the crystallographic axis of the wall lattice.

Recent studies of friction between adsorbed monolayers and smooth crystalline surfaces are relevant to the analysis of flow boundary conditions [54, 55]. It was found that the slip time, which represents the transfer of momentum between the adsorbed monolayer and the substrate, is proportional to the phonon lifetime divided by the normalized peak value of the structure factor computed in the monolayer at the main reciprocal lattice vector [54]. Also, the simulation results have shown that the slip time is independent of the sliding direction if the slip velocity of the monolayer is much smaller than the speed of sound [54]. In the linear regime between friction force and sliding velocity and in the range of film coverages from submonolayer to bilayer, the slip times were computed directly from the decay of the

film velocity and from the decay of the velocity correlation function at equilibrium [55].

During the last two decades, a number of MD studies have examined slip boundary conditions at the interface between *polymeric fluids* and flat crystalline surfaces [40–51]. The velocity profiles with stick boundary conditions were observed when a highly viscous interfacial layer was formed because of the strong wall-fluid interaction [41, 45, 48], high fluid density and pressure [40, 41, 49], or chemical structure of chain molecules [52]. The variation of the slip length as a function of shear rate was reported for flat polymer-solid interfaces with weak wall-fluid interactions [32, 45–47, 49, 50, 53]. In our previous studies [47, 53], it was shown that the rate dependence of the slip length acquires a local minimum at low shear rates followed by a rapid growth at higher shear rates. More recently, a correlation between the shear rate threshold for the boundary slip in dense unentangled polymer films and a chain relaxation dynamics in the interfacial region was reported [49].

In this chapter, we investigate slip boundary conditions at the interface between fluids and crystalline surfaces using molecular dynamics simulations. We find that at sufficiently high shear rates, the slip flow over atomically flat crystalline surfaces is anisotropic. The nonlinear shear rate dependence of the slip length is analyzed in terms of the friction coefficient at the liquid-solid interface and slip velocity. The simulation results indicate that the friction coefficient in the linear slip regime is a function of a single variable that is a product of the height of the normalized main peak in the structure factor and the contact density of the first fluid layer near the solid wall. We will show that the onset of the nonlinear regime between the wall shear stress and slip velocity is determined by the diffusion of fluid monomers within the first layer.

The rest of this chapter is organized as follows. In the next section, we describe the details of molecular dynamics simulations, equilibration procedure, and parameter values for twenty liquid-on-solid systems. The fluid density, velocity and temperature profiles for various flow conditions are discussed in Section III A. The dynamic response of shear viscosity and slip length is examined in Section III B. The numerical analysis of the friction coefficient and induced fluid structure is presented in Section III C. The conclusions are given in the last section.

II. MOLECULAR DYNAMICS SIMULATION MODEL

The geometry of the computational domain and the steady flow profile are shown schematically in Figure 1. The fluid undergoes planar shear flow between two atomically flat walls. For all simulations in this study, the fluid phase consists of $N_f = 9600$ monomers. The interaction between any two fluid monomers is modeled via the truncated Lennard-Jones (LJ) potential

$$V_{LJ}(r) = 4\,\varepsilon\left[\left(\frac{\sigma}{r}\right)^{12} - \left(\frac{\sigma}{r}\right)^{6}\right] \quad \text{for } r \leqslant r_c = 2.5\,\sigma, \tag{1}$$

where ε and σ are the energy and length scales of the fluid phase. The interaction between wall atoms and fluid monomers is also modeled by the LJ potential with parameters $\varepsilon_{\rm wf}$ (the values $\varepsilon_{\rm wf}$ for each system are listed in Table I) and $\sigma_{\rm wf} = \sigma$. The wall atoms do not interact with each other.

Three types of fluid were considered in the present study, i.e., monatomic (or simple) fluid and polymer melts with the number of monomers per chain $N = 10$ and $N = 20$. In the case of polymers, the nearest-neighbor monomers in a chain interact through the finitely extensible nonlinear elastic (FENE) potential [56]

$$V_{FENE}(r) = -\frac{k_s}{2}\,r_o^2\ln[1 - r^2/r_o^2], \tag{2}$$

with the standard choice of parameters $k_s = 30\,\varepsilon\sigma^{-2}$ and $r_o = 1.5\,\sigma$ [57]. As an example, a snapshot of an unentangled polymer melt with linear flexible chains $N = 20$ confined between solid walls is presented in Fig. 2.

The heat exchange between the fluid phase and the external heat bath was regulated via a Langevin thermostat [58], which was applied only to the direction of motion perpendicular to the plane of shear [18]. The equations of motion for fluid monomers in all three directions are given as follows:

$$m\ddot{x}_i = -\sum_{i\neq j}\frac{\partial V_{ij}}{\partial x_i}\,, \tag{3}$$

$$m\ddot{y}_i + m\Gamma\dot{y}_i = -\sum_{i\neq j}\frac{\partial V_{ij}}{\partial y_i} + f_i\,, \tag{4}$$

$$m\ddot{z}_i = -\sum_{i\neq j}\frac{\partial V_{ij}}{\partial z_i}\,, \tag{5}$$

where the summation is performed over the fluid monomers and wall atoms within the cutoff radius $r_c = 2.5\,\sigma$, $\Gamma = 1.0\,\tau^{-1}$ is the friction coefficient, and f_i is a random force

with zero mean and variance $\langle f_i(0) f_j(t) \rangle = 2mk_BT\Gamma\delta(t)\delta_{ij}$ determined from the fluctuation-dissipation theorem. The Langevin thermostat temperature is $T = 1.1\,\varepsilon/k_B$, where k_B is the Boltzmann constant. The equations of motion were integrated using the fifth-order Gear predictor-corrector algorithm [59] with a time step $\triangle t = 0.002\,\tau$, where $\tau = \sqrt{m\sigma^2/\varepsilon}$ is the characteristic time of the LJ potential. The small time step $\triangle t = 0.002\,\tau$ was used in our previous studies [25, 26, 47, 49, 51] for similar MD setups in order to compute accurately the trajectories of fluid molecules and wall atoms near interfaces. Typical values for liquid argon are $\sigma = 0.34\,\text{nm}$, $\varepsilon/k_B = 120\,\text{K}$ and $\tau = 2.16 \times 10^{-12}\,\text{s}$ [59].

Each confining wall is composed of 1152 atoms arranged in two layers of either face-centered cubic (fcc) or body-centered cubic (bcc) lattices. The wall density, lattice type, its orientation with respect to the shear flow direction, and wall-fluid interaction energy are listed in Table I. The wall atoms are either fixed at the lattice sites or allowed to oscillate about their equilibrium lattice positions under the harmonic potential $V_{sp} = \frac{1}{2}\,\kappa\,(r - r_{eq})^2$ with the spring stiffness coefficient $\kappa = 1200\,\varepsilon/\sigma^2$. It was previously shown that this value of the stiffness coefficient does not significantly affect the shear rate dependence of the slip length [26]. In case of thermal walls, the Langevin thermostat was applied to the $\hat{x}$, $\hat{y}$, and $\hat{z}$ components of the wall atom equations of motion. For example, the $\hat{x}$ component of the equation of motion is given by

$$m_w\,\ddot{x}_i + m_w\,\Gamma\dot{x}_i \;=\; -\sum_{i\neq j}\frac{\partial V_{ij}}{\partial x_i} - \frac{\partial V_{sp}}{\partial x_i} + f_i\,, \tag{6}$$

where $m_w = 10\,m$, the friction coefficient is $\Gamma = 1.0\,\tau^{-1}$ and the sum is taken over the neighboring fluid monomers within the cutoff radius $r_c = 2.5\,\sigma$. With these parameters, the oscillation time $2\pi\sqrt{m_w/\kappa} \approx 0.6\,\tau$ of wall atoms is much larger than the integration time step $\triangle t = 0.002\,\tau$. Periodic boundary conditions were imposed along the $\hat{x}$ and $\hat{y}$ directions parallel to the confining walls.

Initially, the fluid was equilibrated at a constant normal pressure applied on the upper wall (shown in Table I) for about $5 \times 10^4\tau$ while the lower wall was at rest. Then, the channel height was fixed and the system was additionally equilibrated for $5 \times 10^4\tau$ at a constant density ensemble while both walls were at rest. The steady flow was generated by moving the upper wall with a constant speed U in the $\hat{x}$ direction parallel to the immobile lower wall (see Fig. 1). The lowest speed of the upper wall is $U = 0.05\,\sigma/\tau$. Both fluid velocity and density profiles were computed within horizontal bins of thickness $\Delta z = 0.01\,\sigma$ for time

intervals up to $6 \times 10^5 \tau$. An estimate of the Reynolds number at the highest shear rates considered in the present study is $O(10)$, which is indicative of laminar flow conditions.

III. RESULTS

A. Fluid density, velocity, and temperature profiles

In this section we present typical fluid density, velocity, and temperature profiles for the polymer system $N = 20$ (system 5 in Table I). First, the averaged fluid density and velocity profiles are displayed in Fig. 3 for the upper wall speeds $U = 0.5\,\sigma/\tau$ and $U = 4.0\,\sigma/\tau$. Notice that the density profiles exhibit a typical layered structure which extends for about $5\,\sigma - 6\,\sigma$ away from the solid walls. The amplitude of the first peak in the density profile determines the contact density ρ_c, an important parameter, which will be used in the subsequent analysis. We emphasize that the thickness of the averaging bins $\Delta z = 0.01\,\sigma$ is small enough so that the value of the contact density does not depend on the bin thickness and bin location relative to the walls. On the other hand, the shape of the density profiles will remain unchanged if thinner bins are used; however, the averaging will require additional computational resources. As evident from Fig. 3 (b), the contact density is reduced at the higher upper wall speed.

The representative velocity profiles normalized by the upper wall speed are shown in Fig. 3 (a) for the same flow conditions as in Fig. 3 (b). It is apparent that the slip velocity is larger at the higher upper wall speed. It should be mentioned that simulations were performed at sufficiently low shear rates so that the fluid slip velocities remained the same at the lower and upper walls. In our study, the location of the liquid-solid interface (marked by the dashed vertical lines in Fig. 3) is defined at the distance $0.5\,\sigma$ away from the wall lattice planes to take into account the excluded volume due to wall atoms. The slip length was computed from the linear fit to the velocity profiles excluding regions of about $2\,\sigma$ from the solid walls, where a slight nonlinearity appears due to fluid layering. At all shear rates examined in the present study, the velocity profiles are linear across the channel and the slip length is larger than about $3\,\sigma$.

In steady flow, the fluid temperature was estimated from the local kinetic energy as

follows:

$$k_B T = \frac{m}{3N} \sum_{i=1}^{N} [\, \dot{\mathbf{r}}_i - \mathbf{v}(\mathbf{r}_i) \,]^2, \tag{7}$$

where $\dot{\mathbf{r}}_i$ is the instantaneous velocity of the fluid monomer and $\mathbf{v}(\mathbf{r}_i)$ is the local flow velocity averaged inside a narrow bin. Averaged temperature profiles across the channel are shown in Fig. 4 for selected values of the upper wall speed. At relatively low shear rates, $\dot{\gamma} \lesssim 0.01\,\tau^{-1}$, the fluid temperature is equal to its equilibrium value of $T = 1.1\,\varepsilon/k_B$ set by the Langevin thermostat. With a further increase of the shear rate, the fluid heats up and the temperature profile in steady state becomes non-uniform across the channel. As seen in Fig. 4, the fluid temperature is higher near the interfaces because of the large slip velocity, which becomes comparable to the thermal velocity, $v_T^2 = k_B T/m$, at high shear rates. We also found that at high shear rates, the temperature in the $\hat{y}$ direction, in which the Langevin thermostat is applied, is slightly smaller than its value in the $\hat{x}$ and $\hat{z}$ directions (shown in the inset of Fig. 4). This difference implies that the kinetic energy in the $\hat{y}$ direction dissipates faster than the energy transfer from the other directions. Similar temperature profiles for a system of linear polymer chains $N = 20$, fluid density $\rho = 0.91\,\sigma^{-3}$, and thermal walls with density $\rho_w = 1.40\,\sigma^{-3}$ were reported in the previous MD study [47]. Further discussion on the relation between temperature profiles and slip velocity in thin polymer films can be found in Ref. [60].

B. Shear viscosity and slip length

The fluid viscosity was estimated from the relation between shear rate and shear stress, which was computed using the Kirkwood formula [61]. The variation of viscosity as a function of shear rate is presented in Fig. 5 for selected systems listed in Table I. In agreement with previous studies with a similar setup [25–27], the viscosity of monatomic fluids is independent of shear rate and equals $\mu = (2.2 \pm 0.2)\ \varepsilon\tau\sigma^{-3}$ when the fluid density is $\rho = 0.81\,\sigma^{-3}$. As expected, the shear viscosity of polymer melts with chains $N = 10$ and $N = 20$ is higher than the viscosity of simple monatomic fluids. For similar flow conditions, the transition from a Newtonian to a shear-thinning flow regime occurs at lower shear rates for polymers with longer chains $N = 20$ because of their slower relaxation dynamics. The slope of the shear-thinning region -0.37, which is shown in Fig. 5 by the dashed line, is consistent with the results reported in earlier studies for polymer melts $N = 20$ at different fluid densi-

ties [47, 49]. As usual, the errors arising from averaging over thermal fluctuations are greater at lower shear rates.

The nonlinear rate dependence of the slip length is shown in Fig. 6 for polymer melts with chains $N = 10$ and $N = 20$. The shear flow direction is oriented along the crystallographic axis of the (111) plane of the fcc wall lattice for systems 6 and 8 (see Table I). In contrast, the fcc lattice plane is rotated by 90° with respect to the flow direction for systems 5 and 7 as indicated by open circles and the blue vertical arrow in the inset of Fig. 6. At low shear rates $\dot{\gamma}\tau \lesssim 0.02$, the slip length is independent of the wall lattice orientation relative to the shear flow direction; while at higher shear rates, the slip length is greater when the shear flow is parallel to the crystallographic axis of the triangular lattice. The same trend for the slip length is observed for monatomic fluids (not shown). These results demonstrate that at sufficiently high shear rates the slip flow is anisotropic even for atomically flat crystalline surfaces.

The appearance of the local minimum in the shear rate dependence of the slip length reported in Fig. 6 for polymer melts with chains $N = 20$ can be explained using simple arguments. The initial decay of the slip length at low shear rates is associated with a slight decrease of the polymer melt viscosity. In this regime, the friction coefficient at the liquid-solid interface (defined as $k = \mu/L_s$) remains constant and independent of shear rate (or slip velocity). With increasing shear rate, both the friction coefficient and polymer viscosity decrease; however, their ratio, the slip length, $L_s = \mu/k$ grows rapidly because of the strong dependence of the friction coefficient on the slip velocity (see also next section). Similar behavior of the slip length for polymer chains $N = 20$ was reported in recent MD studies [47, 53]. Furthermore, the transition to the shear-thinning regime occurs at higher shear rates for polymer melts with shorter chains $N = 10$, and, therefore, the slip length remains nearly constant at low shear rates and then increases rapidly at higher rates (see inset in Fig. 6). These results agree well with the previous simulation results for slip flow of polymers with chain lengths $N \leqslant 16$ and lower fluid density [46].

C. Friction coefficient versus slip velocity

It is difficult to make further progress in the analysis of the shear rate dependent slip length without taking into account shear-thinning effects explicitly. Instead, it is advan-

tageous to reformulate the boundary conditions in terms of the friction coefficient at the liquid-solid interface and slip velocity. In steady shear flow, the shear stress in the bulk of the film ($\dot{\gamma}\mu$) is equal to the wall shear stress (kV_s). In addition, if velocity profiles are linear across the channel, then by definition $V_s = \dot{\gamma} L_s$ and the friction coefficient is given by $k = \mu/L_s$. In what follows, the MD data for the slip length and shear viscosity will be used to compute the friction coefficient, and its dependence on the slip velocity will be investigated.

We next briefly review the results from previous MD studies on slip flows of polymer melts with chains $N = 20$ confined by atomically flat walls with weak surface energy [47, 49]. It was found that in the range of fluid densities $0.86 \leqslant \rho\,\sigma^3 \leqslant 1.02$, the velocity profiles across the channel are linear at all shear rated examined [47]. Therefore, the friction coefficient was computed from the relation $k = \mu/L_s$ and studied as a function of the slip velocity. The data for different fluid densities could be well fitted by the following equation:

$$k/k^* = [1 + (V_s/V_s^*)^2]^{-0.35}, \tag{8}$$

where k^* is the friction coefficient at small slip velocities when $V_s \ll V_s^*$ and V_s^* is the characteristic slip velocity that marks the onset of the nonlinear regime [47]. In the subsequent study [49], the simulations were performed at higher polymer densities, $1.04 \leqslant \rho\,\sigma^3 \leqslant 1.11$, while the rest of the system parameters were kept unchanged. Due to the formation of a highly viscous interfacial layer, the velocity profiles at low shear rates acquired a pronounced curvature near solid walls; and, as a result, the definition $k = \mu/L_s$ could not be applied [49]. Therefore, the friction coefficient was computed directly from the ratio of the wall shear stress and slip velocity of the first fluid layer. Interestingly, for polymer melt densities $\rho = 1.04\,\sigma^{-3}$ and $1.06\,\sigma^{-3}$, the data were again well described by Eq. (8), while at higher melt densities ($1.08 \leqslant \rho\,\sigma^3 \leqslant 1.11$) only the nonlinear regime ($k \sim V_s^{-0.7}$) was observed [49]. We finally note that when the functional form of the slip length versus shear rate reported for monatomic fluids [27] is expressed in terms of k and V_s, the friction coefficient is also well fitted by Eq. (8) in the range $k/k^* \gtrsim 0.3$ [47].

We extend the analysis of the friction coefficient at liquid-solid interfaces, which are described by the parameters listed in Table I. Figure 7 shows the friction coefficient as a function of the slip velocity normalized by the parameters k^* and V_s^* respectively. Remarkably, the data for all twenty systems in Table I are well fitted by Eq. (8) over about

three orders of magnitude. These results further support our previous conclusions that the boundary condition Eq. (8) describes slip flows of both monatomic and polymeric fluids over smooth solid walls. We also noticed the inverse correlation between the friction coefficient k^* and the characteristic slip velocity V_s^*, which is summarized in Fig. 8. Note that for every two systems, where the only difference is the orientation of the fcc wall lattice, the values of k^* are nearly the same, but the slip velocity V_s^* is slightly smaller when the shear flow direction is parallel to the crystallographic axis. This is consistent with the dynamic response of the slip length reported in Fig. 6 for two different orientations of the fcc lattice; namely, the onset of rapid growth of the slip length occurs at smaller shear rates when the the flow is oriented along the crystallographic axis.

We next argue that the onset of the nonlinear regime in Eq. (8) is determined by the diffusion time of fluid monomers over the distance between the nearest minima of the periodic surface potential. In the absence of shear flow, the typical trajectories of fluid monomers in the first layer near the solid wall are presented in Fig. 9. It can be observed that the diffusive motion of fluid monomers in contact with the lower wall atoms is strongly influenced by the corrugation of the surface potential; i.e., most of the time the monomer resides near the local minima of the surface potential with occasional jumps between the minima. Therefore, the elementary relaxation time within the first fluid layer can be estimated from the diffusion of monomers over the distance between the nearest minima.

In Figure 10 we plot the mean square displacement curves for fluid monomers within the first layer for selected systems in Table I at equilibrium (i.e., when both walls are at rest). The displacement vector as a function of time was computed along the trajectory of a fluid monomer only if it remained in the first layer during the time interval between successive measurements of the monomer position. Note that for monatomic fluids, there is a linear dependence between the mean square displacement and time, and, consequently, the diffusion coefficient is well defined by the Einstein relation. In contrast, fluid monomers that belong to a polymer chain diffuse slower than monomers in simple fluids since their dynamics is bounded by diffusion of the center of mass of the polymer chain. It should be mentioned that the evaluation of the mean square displacement curves at large times requires significant computational resources because of the low probability that a fluid monomer will remain within the first layer for a long time interval. The slope of the subdiffusive regime at intermediate times is indicated by the straight dashed line in Fig. 10.

Finally, the comparison of the characteristic slip time of the first fluid layer in steady shear flow and the diffusion time of fluid monomers between nearest minima of the surface potential at equilibrium is presented in Fig. 11. The diffusion time was estimated from the mean square displacement of fluid monomers within the first layer at the distance between nearest minima of the periodic surface potential. The same distance divided by the slip velocity V_s^* defines the characteristic slip time of the first fluid layer. In the case when the shear flow direction is parallel to the $[1\bar{1}0]$ fcc lattice orientation (indicated by the vertical blue arrow in the inset of Fig. 6), the slipping distance of the first layer was computed by projecting the vector, which connects the nearest minima of the surface potential, onto the direction of flow. As seen in Figure 11, there is a strong correlation between the characteristic slip time of the first fluid layer and the diffusion time of fluid monomers in that layer at equilibrium. These results indicate that the linear relation between the wall shear stress and slip velocity in Eq. (8) holds when the slip velocity is smaller than the diffusion velocity of fluid monomers in contact with crystalline surfaces.

D. Friction coefficient and induced fluid structure

The fluid structure near flat solid walls is characterized by density layering perpendicular to the surface and ordering of fluid monomers within the layers [62]. Examples of oscillatory density profiles in a polymer melt near confining walls were presented in Fig. 3. It is intuitively expected that enhanced fluid density layering normal to the surface (obtained, for example, by increasing fluid pressure or wall-fluid interaction energy) would correspond to a larger friction coefficient at the liquid-solid interface. However, this correlation does not always hold; for example, the amplitude of fluid density oscillations near flat structureless walls might be large, but the friction coefficient is zero. As emphasized in the original paper by Thompson and Robbins [18], the surface-induced fluid ordering within the first layer of monomers correlates well with the degree of slip at the liquid-solid interface. The measure of the induced order in the adjacent fluid layer is the static structure factor, which is defined as follows:

$$S(\mathbf{k}) = \frac{1}{N_\ell} \left| \sum_{j=1}^{N_\ell} e^{i\,\mathbf{k}\cdot\mathbf{r}_j} \right|^2, \tag{9}$$

where $\mathbf{k}$ is a two-dimensional wave vector, $\mathbf{r}_j = (x_j, y_j)$ is the position vector of the jth monomer, and $N_\ell = S(0)$ is the number of monomers within the layer [18]. The probability of finding fluid monomers is greater near the minima of the periodic surface potential; and, therefore, the structure factor typically contains a set of sharp peaks at the reciprocal lattice vectors. It is well established that the magnitude of the largest peak at the first reciprocal lattice vector is one of the main factors that determines the value of the slip length at the interface between flat crystalline surfaces and monatomic fluids [18, 21, 25, 26] or polymer melts [40, 46, 47, 49].

Next, we discuss the influence of the wall-fluid interaction energy, wall lattice type and orientation, and slip velocity on the structure factor computed in the first fluid layer. First, the effect of the wall-fluid interaction energy is illustrated in Fig. 12 for monatomic fluids in contact with the (111) plane of the fcc wall lattice. The height of the surface-induced peaks in the structure factor is slightly larger at higher surface energy. The magnitude of the peak in the shear flow direction is $S(8.65\,\sigma^{-1}, 0) = 0.98$ for $\varepsilon_{\rm wf} = 0.3\,\varepsilon$ and $S(8.65\,\sigma^{-1}, 0) = 1.06$ for $\varepsilon_{\rm wf} = 0.4\,\varepsilon$. Notice that the height of the circular ridge, which is characteristic of short range order of fluid monomers, is larger than the amplitude of the induced peaks at the main reciprocal lattice vectors. A similar trend in the height of the peaks in the structure factor was observed previously for monatomic fluids near fcc walls with higher density $\rho_w = 2.73\,\sigma^{-3}$ [25].

Figure 13 shows the structure factor computed in the first fluid layer for polymer melts with chains $N = 20$ in contact with the (111) plane of the fcc wall lattice. As indicated by the horizontal arrows, the shear flow is oriented along the $[11\bar{2}]$ direction in Fig. 13 (a) and parallel to the $[1\bar{1}0]$ direction in Fig. 13 (b). Due to the hexagonal symmetry of the (111) lattice plane, the structure factor exhibits six peaks at the shortest reciprocal lattice vectors. Note that only two main peaks are present in the first quadrant. The magnitude of the peaks is the same at small slip velocities. The lattice orientation with respect to the shear flow direction determines the location of the main peaks.

Lastly, the effect of slip velocity on the magnitude of the substrate-induced peaks in the structure factor is presented in Fig. 14 for polymer chains in contact with the (001) plane of the bcc wall lattice. In the case of small slip velocity $V_s = 0.012\,\sigma/\tau$, the magnitude of the main peaks at the main reciprocal lattice vectors $\mathbf{G}_1 = (6.18\,\sigma^{-1}, 0)$ and $\mathbf{G}_2 = (0, 6.18\,\sigma^{-1})$ is the same [see Fig. 14 (a)]. With increasing slip velocity, the height of the induced peak

along the shear flow direction decreases significantly, whereas the amplitude of the peak in the perpendicular direction is less affected by the slip velocity [see Fig. 14 (b)]. More qualitatively, the velocity dependence of the main peaks in the structure factor along with the contact density and temperature of the first layer are presented in Fig. 15. This behavior is consistent with the density and temperature profiles reported in Section III A. Similar conclusions were obtained in the previous study on slip flows in dense polymer films [49].

The correlation between surface-induced structure in the first fluid layer and the friction coefficient was investigated previously for polymer melts with chains $N = 20$ confined by atomically flat walls [47, 49]. The simulations were performed at fluid densities $0.86 \leqslant \rho\,\sigma^3 \leqslant 1.11$ and the wall density $\rho_w = 1.40\,\sigma^{-3}$. It was found that the data for the friction coefficient at different shear rates and fluid densities collapsed onto a master curve when plotted as a function of a variable $S(0)/[S(\mathbf{G}_1)\,\rho_c]$, where $\mathbf{G}_1$ is the first reciprocal lattice vector in the shear flow direction [47, 49]. The collapse of the data holds at relatively small values of the friction coefficient $k \lesssim 4\,\varepsilon\tau\sigma^{-4}$ and for slip lengths larger than approximately $5\,\sigma$. Although these results are promising, the simulations were limited to a single wall density and the $[11\bar{2}]$ orientation of the (111) plane of the fcc wall lattice. Therefore, it is desirable to perform additional simulations in a more extended parameter range.

In the present study, a number of parameters that affect slippage at the liquid-solid interface have been examined, i.e., fluid and wall densities, polymer chain length, wall lattice type and orientation, wall-fluid interaction energy, thermal and solid walls (see Table I). We first consider the linear-response regime where the friction coefficient weakly depends on the slip velocity ($k/k^* \gtrsim 0.8$ in Fig. 7). Figure 16 shows the ratio L_s/μ (an inverse friction coefficient) as a function of the variable $S(0)/[S(\mathbf{G}_1)\,\rho_c]$ computed in the first fluid layer for twenty systems listed in Table I. In the case when the shear flow direction is parallel to the $[1\bar{1}0]$ orientation of the fcc lattice [e.g., see Fig. 13 (b)], the structure factor was computed at the shortest reciprocal lattice vector $\mathbf{G}_1$ aligned at an angle of 30° with respect to the $\hat{x}$ axis. The data in Fig. 7 are well described by a power-law fit with the slope 1.13. Remember also that the amplitude of the main peaks in the structure factor and the contact density of the first fluid layer are the same at equilibrium and small slip velocities (e.g., see Fig. 15). Therefore, the results in Fig. 16 suggest that at the interface between simple or polymer fluids and crystalline surfaces, the ratio of the slip length and fluid viscosity at low shear rates can be predicted from equilibrium measurements of the structure factor and

contact density of the first fluid layer. In other words, the value of parameter k^* in Eq. (8) is determined by the induced fluid structure in the first layer at equilibrium.

In Figure 17 we report the dependence of the friction coefficient ($k = \mu/L_s$) on the structure factor and contact density of the first fluid layer at all shear rates examined in this study. These results call for several comments. Note that at higher shear rates the derivative of L_s/μ with respect to the variable $S(0)/[S(\mathbf{G}_1)\,\rho_c]$ for several systems listed in Table I deviates significantly from the slope 1.13, which is indicated by a straight line in Fig. 17 (a). In addition, for any two systems with the same ρ_w and $\varepsilon_{\rm wf}$, the ratio L_s/μ as a function of $S(0)/[S(\mathbf{G}_1)\,\rho_c]$ depends on the orientation of the fcc wall lattice with respect to the shear flow direction. Although the data in Fig. 17 (b) are somewhat scattered, the results show the same trend; namely, the friction coefficient decreases when the magnitude of the normalized peak in the structure factor is reduced. The collapse of the data for L_s versus $S(\mathbf{G}_1)/S(0)$ was reported in Ref. [18] for monatomic fluids and crystalline walls when $L_s \lesssim 3.5\,\sigma$ and the boundary conditions are rate independent. In the present study, the slip lengths are greater than about $5\,\sigma$ except for the systems 13 and 16 where $L_s \approx 3\,\sigma$ at low shear rates.

IV. CONCLUSIONS

In summary, we investigated the dynamic behavior of the slip length at interfaces between polymeric or monatomic fluids and dense crystalline surfaces using molecular dynamics simulations. The polymer melt was modeled as a collection of bead-spring linear flexible chains well below the entanglement length. We considered shear flow conditions at relatively low fluid densities (pressures) and weak wall-fluid interaction energies so that fluid velocity profiles are linear across the channel and slip lengths are larger than several molecular diameters at all shear rates examined. The simulations were performed for different wall and fluid densities, chain lengths, surface energies, lattice types, thermal or solid walls. It was found that the slip length does not depend on the wall lattice orientation with respect to the flow direction only at low shear rates, whereas the slip is enhanced at high shear rates when the flow direction is parallel to the crystallographic axis of the substrate.

We reformulated the boundary conditions in terms of the friction coefficient at the liquid-solid interface and slip velocity. It was shown that in the steady shear flow of either monatomic fluids or polymer melts, the friction coefficient undergoes a transition from a

constant value to the power-law decay as a function of the slip velocity. The numerical results indicate that the characteristic velocity of the transition is determined by the diffusion time of fluid monomers over the distance between nearest minima of the substrate potential. It was demonstrated that the friction coefficient at small slip velocities is a function of the magnitude of the surface-induced peak in the structure factor and the contact density of the first fluid layer. These results suggest that the value of the slip length in the low-shear-rate limit can be predicted from equilibrium measurements of the induced structure in the first fluid layer. Future studies will show how general these conclusions are and whether they hold for more realistic potentials or different thermostatting procedures.

Acknowledgments

Financial support from the National Science Foundation (CBET-1033662) and the Petroleum Research Fund of the American Chemical Society (48631-G9) is gratefully acknowledged. Computational work in support of this research was performed at Michigan State University's High Performance Computing Facility.

---

[1] W. Sparreboom, A. van den Berg and J. C. T. Eijkel, Nature Nanotechnology **4**, 713 (2009).

[2] Y. Zhu and S. Granick, Phys. Rev. Lett. **88**, 106102 (2002).

[3] J. Sanchez-Reyes and L. A. Archer, Langmuir **19**, 3304 (2003).

[4] T. Schmatko, H. Hervet, and L. Leger, Langmuir **22**, 6843 (2006).

[5] N. V. Churaev, V. D. Sobolev, and A. N. Somov, J. Colloid Interface Sci. **97**, 574 (1984).

[6] J. Baudry, E. Charlaix, A. Tonck, and D. Mazuyer, Langmuir **17**, 5232 (2001).

[7] T. Schmatko, H. Hervet, and L. Leger, Phys. Rev. Lett. **94**, 244501 (2005).

[8] S. P. McBride and B. M. Law, Phys. Rev. E **80**, 060601(R) (2009).

[9] O. Baumchen, R. Fetzer, and K. Jacobs, Phys. Rev. Lett. **103**, 247801 (2009).

[10] Y. Zhu and S. Granick, Phys. Rev. Lett. **87**, 096105 (2001).

[11] C. H. Choi, K. J. A. Westin, and K. S. Breuer, Phys. Fluids **15**, 2897 (2003).

[12] U. Ulmanella and C.-M. Ho, Phys. Fluids **20**, 101512 (2008).

[13] J. P. Rothstein, Annu. Rev. Fluid Mech. **42**, 89 (2010).

[14] O. Baumchen and K. Jacobs, J. Phys. Condens. Matter **22**, 033102 (2010).

[15] L. Bocquet and E. Charlaix, Chem. Soc. Rev. **39**, 1073 (2010).

[16] U. Heinbuch and J. Fischer, Phys. Rev. A **40**, 1144 (1989).

[17] J. Koplik, J. R. Banavar, and J. F. Willemsen, Phys. Fluids A **1**, 781 (1989).

[18] P. A. Thompson and M. O. Robbins, Phys. Rev. A **41**, 6830 (1990).

[19] L. Bocquet and J.-L. Barrat, Phys. Rev. E **49**, 3079 (1994).

[20] J.-L. Barrat and L. Bocquet, Phys. Rev. Lett. **82**, 4671 (1999).

[21] J.-L. Barrat and L. Bocquet, Faraday Discuss. **112**, 119 (1999).

[22] K. P. Travis and K. E. Gubbins, J. Chem. Phys. **112**, 1984 (2000).

[23] V. P. Sokhan, D. Nicholson, and N. Quirke, J. Chem. Phys. **115**, 3878 (2001).

[24] T. M. Galea and P. Attard, Langmuir **20**, 3477 (2004).

[25] N. V. Priezjev, Phys. Rev. E **75**, 051605 (2007).

[26] N. V. Priezjev, J. Chem. Phys. **127**, 144708 (2007).

[27] P. A. Thompson and S. M. Troian, Nature (London) **389**, 360 (1997).

[28] C. Liu and Z. Li, Phys. Rev. E **80**, 036302 (2009).

[29] N. Asproulis and D. Drikakis, Phys. Rev. E **81**, 061503 (2010).

[30] X. Yong and L. T. Zhang, Phys. Rev. E **82**, 056313 (2010).

[31] A. A. Pahlavan and J. B. Freund, Phys. Rev. E **83**, 021602 (2011).

[32] A. Martini, H. Y. Hsu, N. A. Patankar, and S. Lichter, Phys. Rev. Lett. **100**, 206001 (2008).

[33] S. C. Yang and L. B. Fang, Molecular Simulation **31**, 971 (2005).

[34] A. Niavarani and N. V. Priezjev, Phys. Rev. E **81**, 011606 (2010).

[35] N. V. Priezjev and S. M. Troian, J. Fluid Mech. **554**, 25 (2006).

[36] F. D. Sofos, T. E. Karakasidis, and A. Liakopoulos, Phys. Rev. E **79**, 026305 (2009).

[37] F. Feuillebois, M. Z. Bazant, and O. I. Vinogradova, Phys. Rev. Lett. **102**, 026001 (2009).

[38] N. V. Priezjev, A. A. Darhuber, and S. M. Troian, Phys. Rev. E **71**, 041608 (2005).

[39] C. Y. Soong, T. H. Yen, P. Y. Tzeng, Phys. Rev. E **76**, 036303 (2007).

[40] P. A. Thompson, M. O. Robbins, and G. S. Grest, Israel Journal of Chemistry **35**, 93 (1995).

[41] E. Manias, G. Hadziioannou, and G. ten Brinke, Langmuir **12**, 4587 (1996).

[42] R. Khare, J. J. de Pablo, and A. Yethiraj, Macromolecules **29**, 7910 (1996).

[43] M. J. Stevens, M. Mondello, G. S. Grest, S. T. Cui, H. D. Cochran, and P. T. Cummings, J. Chem. Phys. **106**, 7303 (1997).

[44] A. Koike and M. Yoneya, J. Phys. Chem. B **102**, 3669 (1998).

[45] A. Jabbarzadeh, J. D. Atkinson, and R. I. Tanner, J. Chem. Phys. **110**, 2612 (1999).

[46] N. V. Priezjev and S. M. Troian, Phys. Rev. Lett. **92**, 018302 (2004).

[47] A. Niavarani and N. V. Priezjev, Phys. Rev. E **77**, 041606 (2008).

[48] J. Servantie and M. Muller, Phys. Rev. Lett. **101**, 026101 (2008).

[49] N. V. Priezjev, Phys. Rev. E **80**, 031608 (2009).

[50] S. Dhondi, G. G. Pereira, and S. C. Hendy, Phys. Rev. E **80**, 036309 (2009).

[51] N. V. Priezjev, Phys. Rev. E **82**, 051603 (2010).

[52] L.-T. Kong, C. Denniston, and M. H. Muser, Modelling Simul. Mater. Sci. Eng. **18**, 034004 (2010).

[53] A. Niavarani and N. V. Priezjev, J. Chem. Phys. **129**, 144902 (2008).

[54] E. D. Smith, M. O. Robbins, and M. Cieplak, Phys. Rev. B **54**, 8252 (1996).

[55] M. S. Tomassone, J. B. Sokoloff, A. Widom, J. Krim, Phys. Rev. Lett. **79**, 4798 (1997).

[56] R. B. Bird, C. F. Curtiss, R. C. Armstrong, and O. Hassager, *Dynamics of Polymeric Liquids* 2nd ed. (Wiley, New York, 1987).

[57] K. Kremer and G. S. Grest, J. Chem. Phys. **92**, 5057 (1990).

[58] G. S. Grest and K. Kremer, Phys. Rev. A **33**, 3628 (1986).

[59] M. P. Allen and D. J. Tildesley, *Computer Simulation of Liquids* (Clarendon, Oxford, 1987).

[60] R. Khare, P. Keblinski, and A. Yethiraj, Int. J. Heat Mass Transfer **49**, 3401 (2006).

[61] J. H. Irving and J. G. Kirkwood, J. Chem. Phys. **18**, 817 (1950).

[62] W. D. Kaplan and Y. Kauffmann, Annu. Rev. Mater. Res. **36**, 1 (2006).

Figures

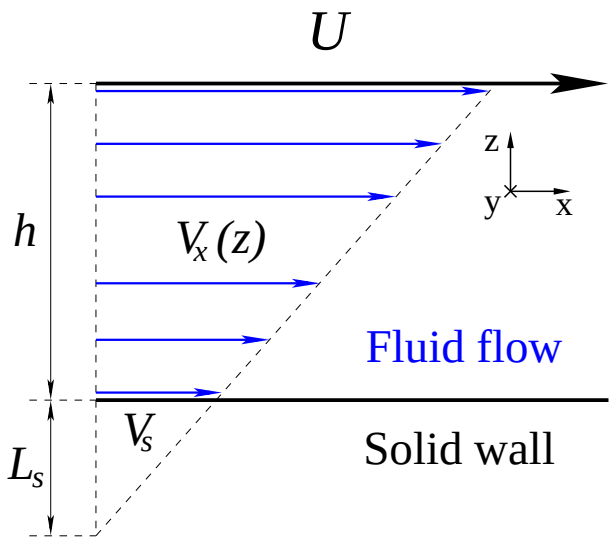

FIG. 1: (Color online) A schematic representation of the flow with slip boundary conditions. The steady shear flow is induced by the upper wall moving with a constant speed U in the $\hat{x}$ direction. The slip velocity and slip length L_s are related via $V_s = \dot{\gamma} L_s$, where $\dot{\gamma}$ is the shear rate computed from the slope of the velocity profile.

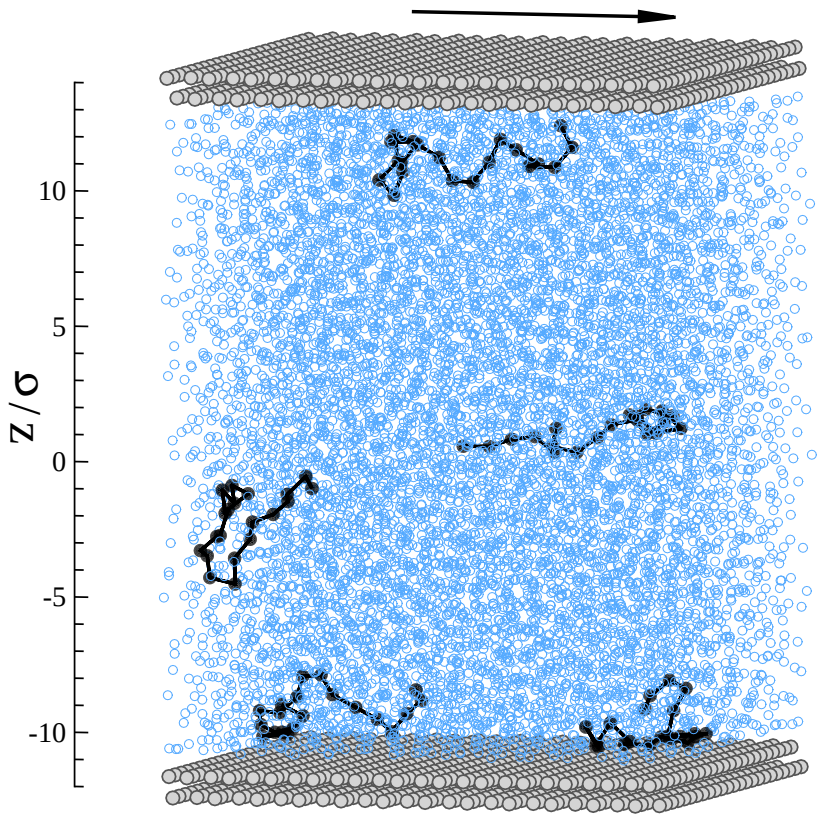

FIG. 2: (Color online) A snapshot of fluid monomers (open blue circles) and wall atoms (filled gray circles) positions. Five polymer chains are marked by solid lines and filled black circles. The black arrow indicates the upper wall velocity $U = 0.5\,\sigma/\tau$ in the $\hat{x}$ direction. The fluid monomer density is $\rho = 0.89\,\sigma^{-3}$ and the wall density is $\rho_w = 1.80\,\sigma^{-3}$. The rest of parameters for the system 5 are given in Table I. Reprinted from [51].

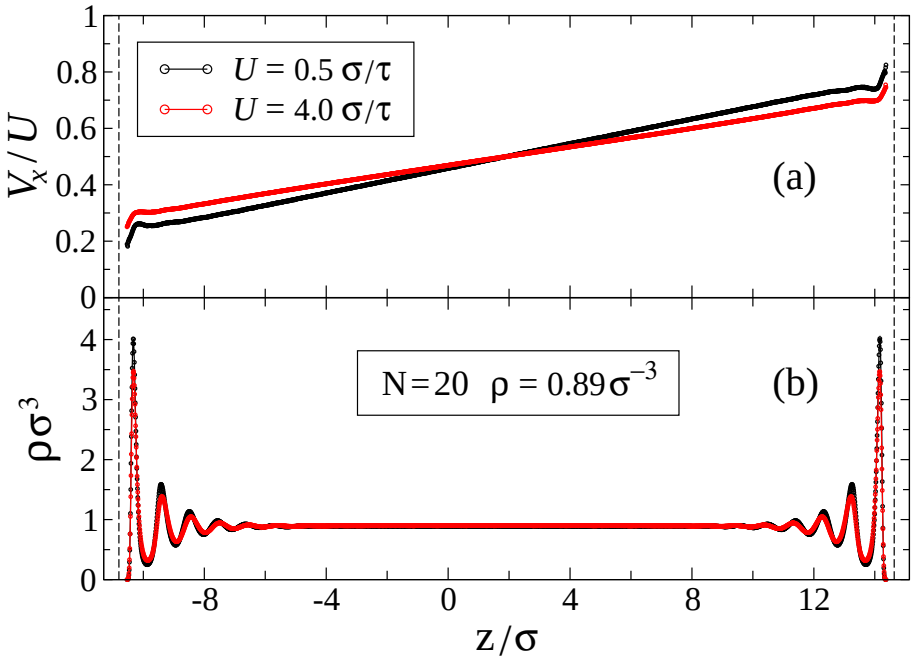

FIG. 3: (Color online) Averaged normalized velocity (a) and density (b) profiles across the channel for the upper wall speeds $U = 0.5\,\sigma/\tau$ and $U = 4.0\,\sigma/\tau$. The uniform monomer density of the polymer melt $N = 20$ away from the walls is $\rho = 0.89\,\sigma^{-3}$ (system 5 in Table I). The vertical axes indicate the location of the fcc lattice planes (at $z/\sigma = -11.30$ and 15.14) in contact with the fluid. The dashed lines at $z/\sigma = -10.80$ and 14.64 denote reference planes for computing the slip length. Reprinted from [51].

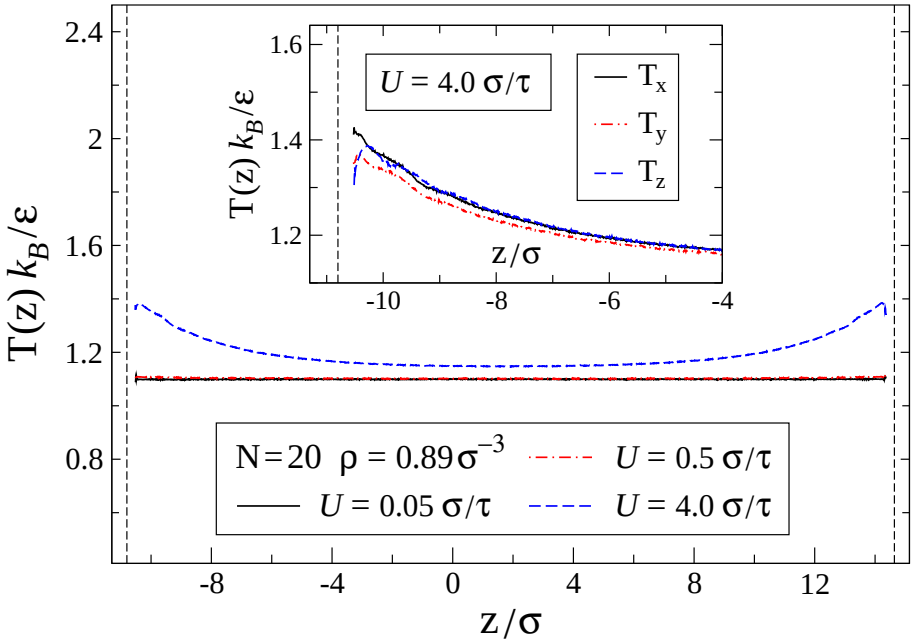

FIG. 4: (Color online) Temperature profiles across the channel for the indicated upper wall velocities (system 5 in Table I). The vertical dashed lines at $z/\sigma = -10.80$ and 14.64 indicate the location of liquid-solid interfaces. The inset shows the $\hat{x}$, $\hat{y}$, and $\hat{z}$ components of the temperature profile near the stationary lower wall when the upper wall velocity is $U = 4.0\,\sigma/\tau$.

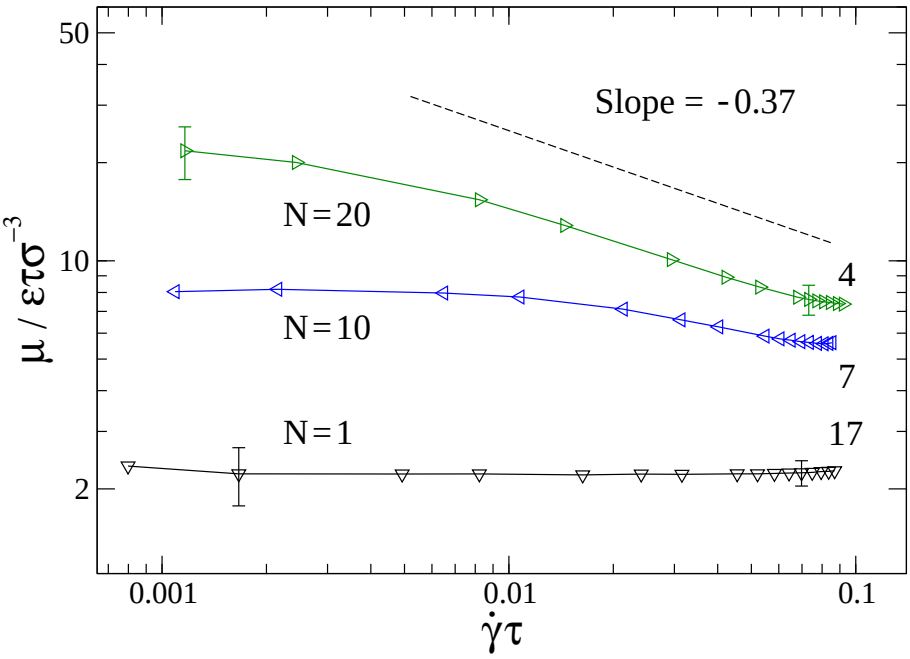

FIG. 5: (Color online) Fluid viscosity μ (in units $\varepsilon\tau\sigma^{-3}$) as a function of shear rate for the indicated systems listed in Table I. The dashed line with a slope -0.37 is shown for reference. Solid curves are a guide for the eye. Adapted from [51].

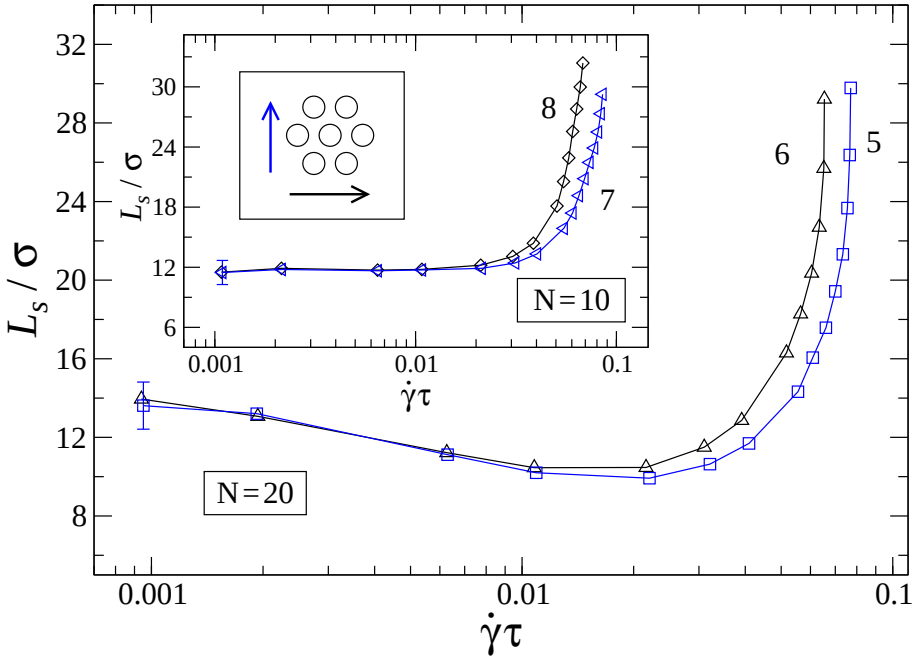

FIG. 6: (Color online) Slip length L_s/σ as a function of shear rate for polymer melts with chains $N = 20$ and $N = 10$ (see inset). The system parameters are listed in Table I. Open circles in the inset represent the (111) face of the fcc lattice atoms in contact with the fluid. The vertical blue arrow indicates the shear flow direction with respect to the $[11\bar{2}]$ fcc lattice orientation (systems 5 and 7). The horizontal black arrow shows the flow direction along the $[1\bar{1}0]$ orientation (systems 6 and 8). Reprinted from [51].

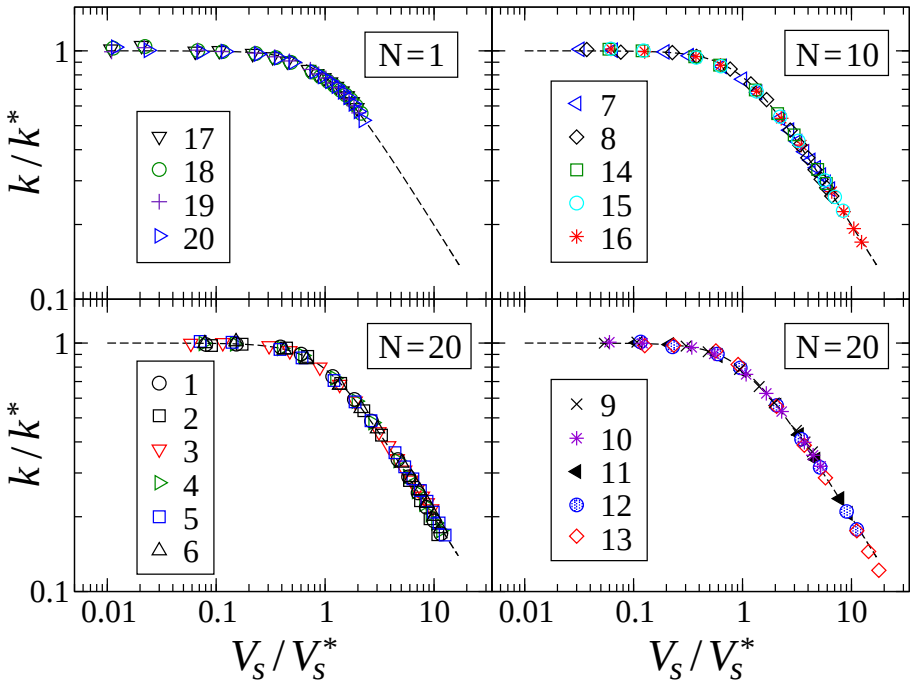

FIG. 7: (Color online) Log-log plot of the friction coefficient $k = \mu/L_s$ (in units $\varepsilon\tau\sigma^{-4}$) as a function of the slip velocity $V_s = L_s\dot{\gamma}$ (in units σ/τ) for systems listed in Table I. The values of the normalization parameters V_s^* and k^* are presented in Fig. 8. The dashed curves $y = (1 + x^2)^{-0.35}$ are the best fit to the data. Reprinted from [51].

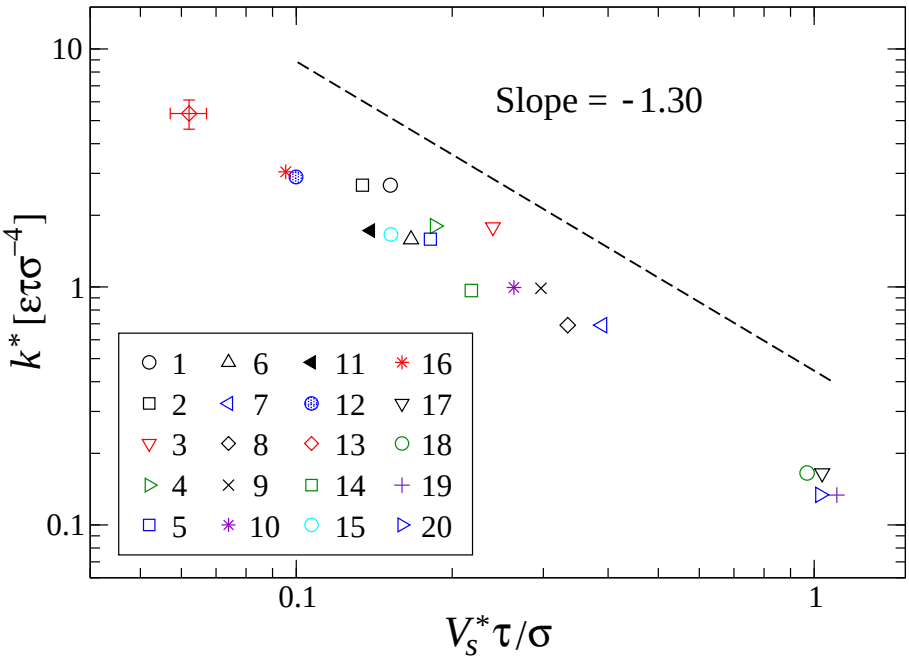

FIG. 8: (Color online) The normalization parameters V_s^* (in units σ/τ) and k^* (in units $\varepsilon\tau\sigma^{-4}$) used to fit the data in Fig. 7 to Eq. (8). The inset shows system indices listed in Table I. The dashed line with a slope -1.30 is shown for reference. Reprinted from [51].

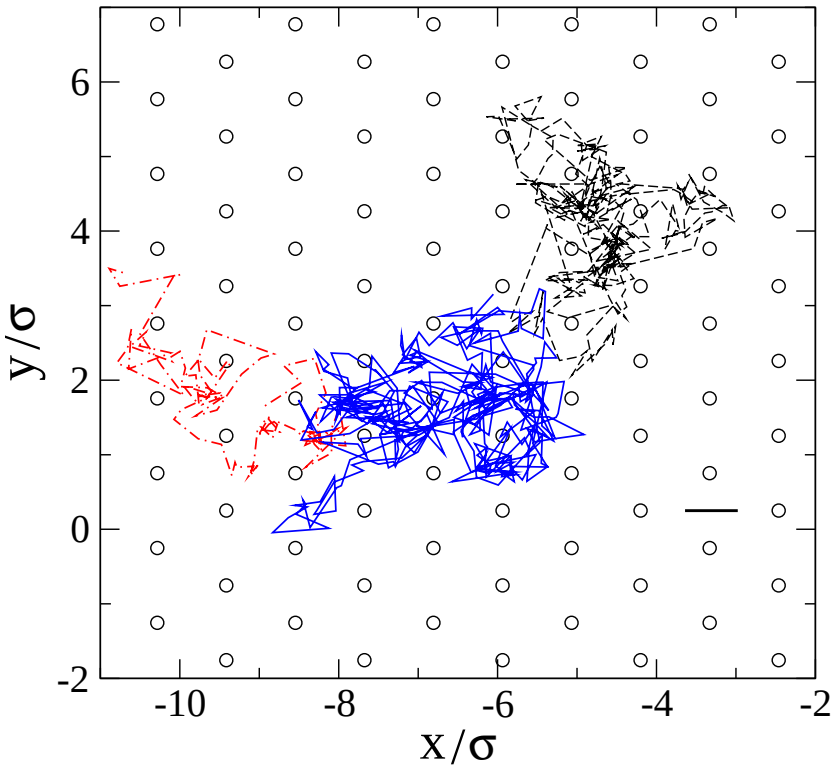

FIG. 9: (Color online) Typical trajectories, projected onto the xy plane, of monomers in the first fluid layer near the lower wall for the system 1 (see Table I) at equilibrium (i.e., when both walls are at rest). The fcc lattice sites of the (111) plane are indicated by open circles. The horizontal line segment denotes the distance between nearest minima of the periodic surface potential.

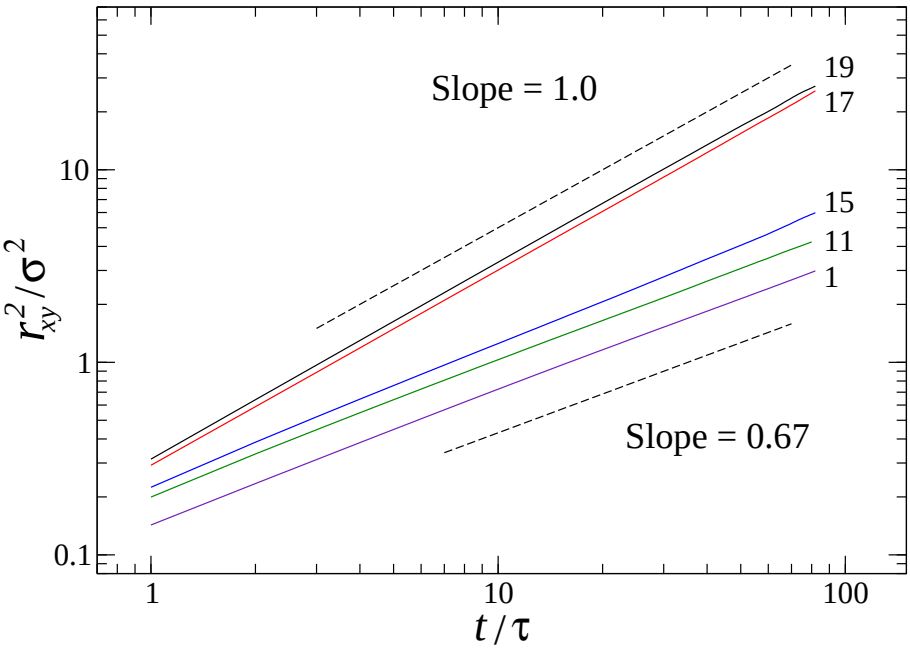

FIG. 10: (Color online) The mean square displacement of monomers in the first fluid layer at equilibrium (i.e., when both walls are at rest) as a function of time for five systems listed in Table I. The dashed lines indicate slopes of 1.0 and 0.67. Adapted from [51].

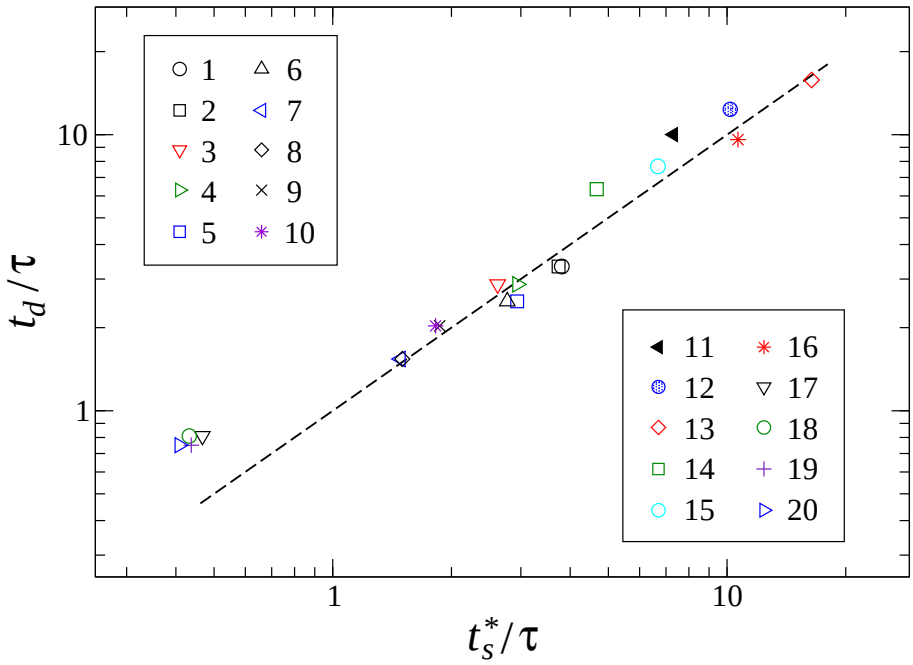

FIG. 11: (Color online) A correlation between the characteristic slip time t_s^* of the first fluid layer and the diffusion time t_d of fluid monomers between nearest minima of the periodic surface potential. The error bars are about the symbol size. The system parameters are listed in Table I. The dashed line $y = x$ is shown as a reference. Adapted from [51].

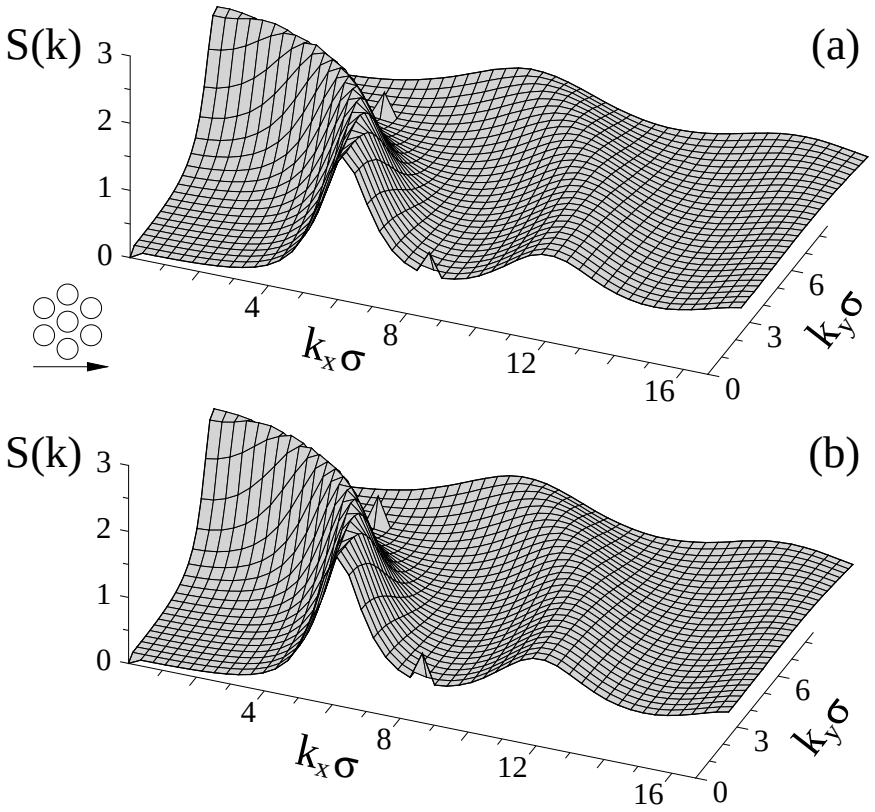

FIG. 12: Two-dimensional structure factor $S(k_x, k_y)$ computed in the first fluid layer for $N = 1$ and $U = 0.05\,\sigma/\tau$ [systems (a) 19 and (b) 17 in Table I]. The wall-fluid interaction energy is (a) $\varepsilon_{\rm wf} = 0.3\,\varepsilon$ and (b) $\varepsilon_{\rm wf} = 0.4\,\varepsilon$. The shear flow direction (denoted by the horizontal arrow) is parallel to the $[11\bar{2}]$ orientation of the (111) face of the fcc wall lattice (open circles). Reprinted from [51].

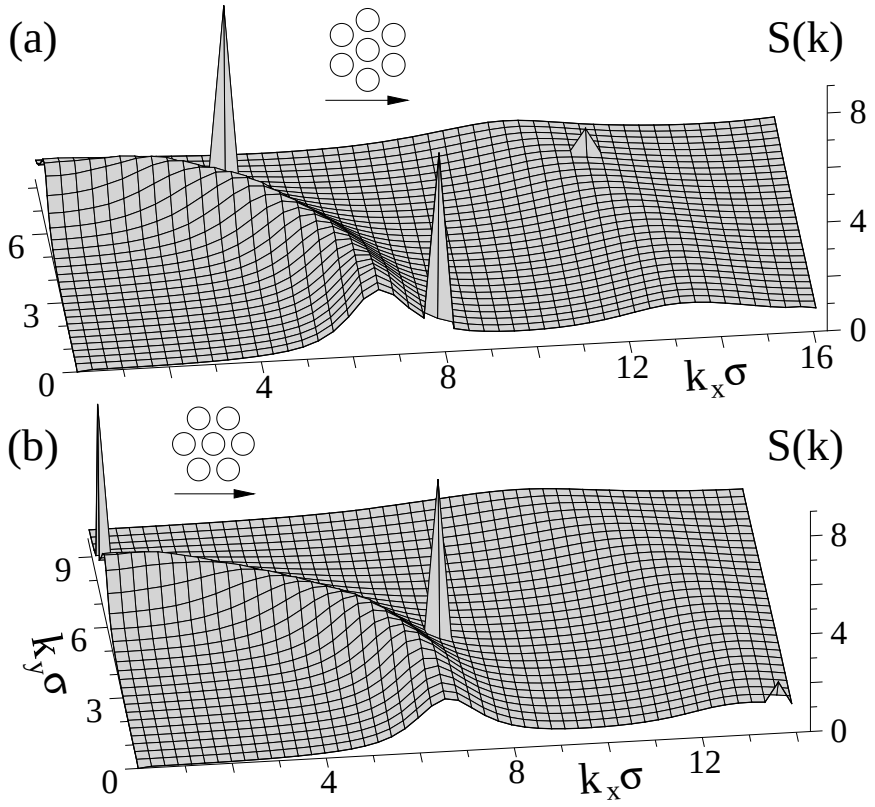

FIG. 13: Structure factor $S(k_x, k_y)$ averaged in the first fluid layer for $N = 20$ polymer systems (a) 5 and (b) 6 (see parameters in Table I). The sharp peaks are located at (a) $(7.86\,\sigma^{-1}, 0)$ and $(3.93\,\sigma^{-1}, 6.81\,\sigma^{-1})$, and (b) $(6.81\,\sigma^{-1}, 3.93\,\sigma^{-1})$ and $(0, 7.86\,\sigma^{-1})$. In each case, horizontal arrows indicate the shear flow direction with respect to the orientation of the (111) plane of the fcc wall lattice (denoted by open circles). The upper wall speed is $U = 0.05\,\sigma/\tau$ in both cases. Adapted from [51].

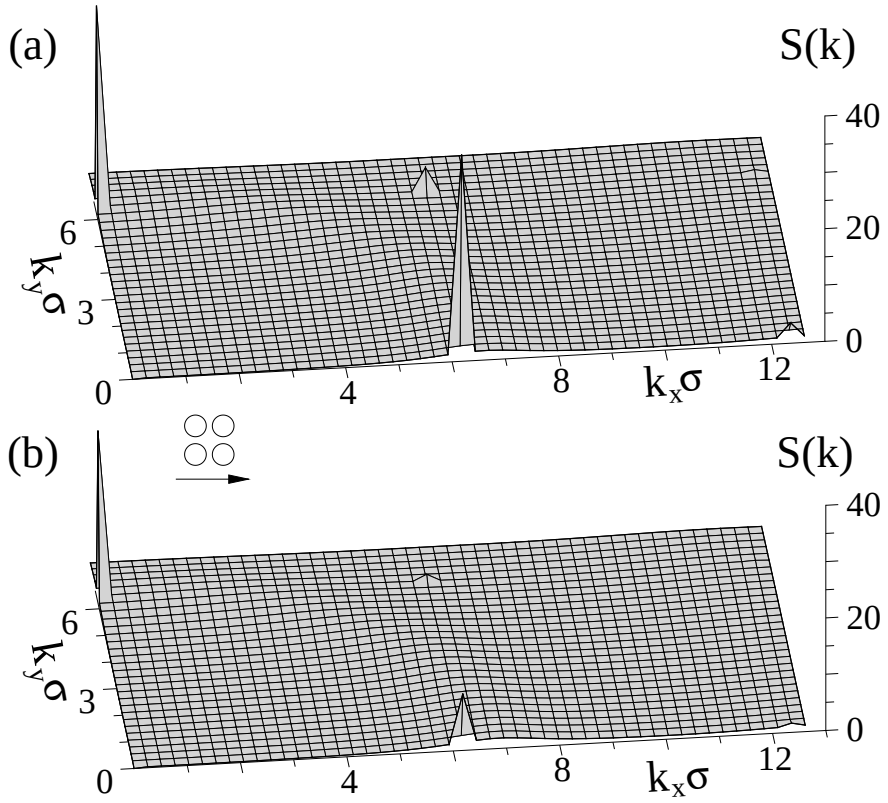

FIG. 14: Structure factor $S(k_x, k_y)$ computed in the first fluid layer for $N = 20$ polymer system 12 (see Table I). The upper wall speed and slip velocity are (a) $U = 0.05\,\sigma/\tau$ and $V_s = 0.012\,\sigma/\tau$ and (b) $U = 2.0\,\sigma/\tau$ and $V_s = 0.51\,\sigma/\tau$ respectively. The location of the main induced peak in the shear direction is $(6.18\,\sigma^{-1}, 0)$. The horizontal arrows denote the shear flow direction with respect to the orientation of the (001) face of the bcc wall lattice (open circles). Reprinted from [51].

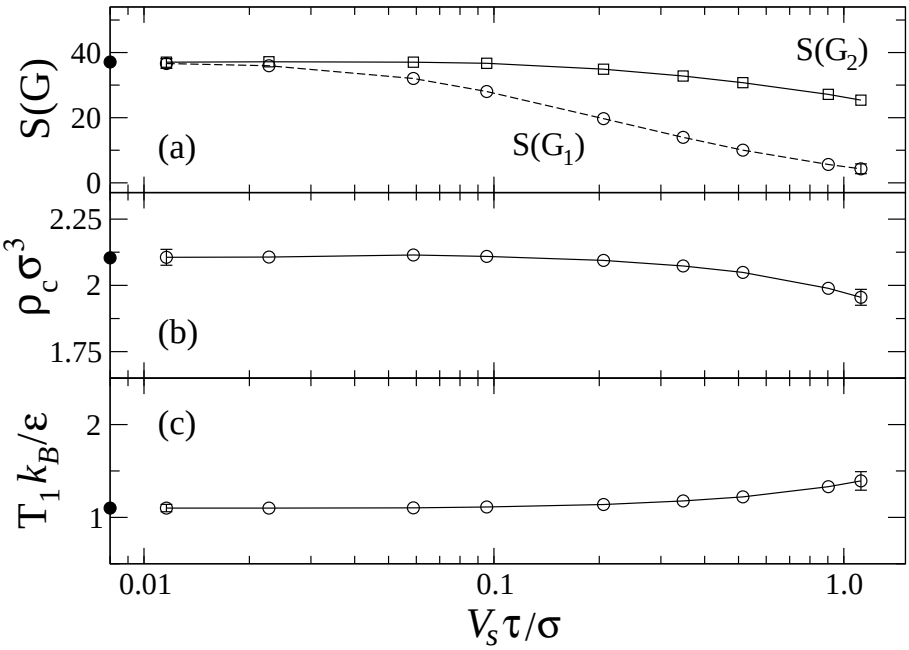

FIG. 15: (a) Structure factor computed at the main reciprocal vectors of the bcc lattice $\mathbf{G}_1 = (6.18\,\sigma^{-1}, 0)$ and $\mathbf{G}_2 = (0, 6.18\,\sigma^{-1})$, (b) contact density, and (c) temperature of the first fluid layer as a function of the slip velocity $V_s = L_s\dot{\gamma}$ for polymer chains $N = 20$ (system 12 in Table I). The same parameters at equilibrium (i.e., when $V_s = 0$) are denoted by closed symbols.

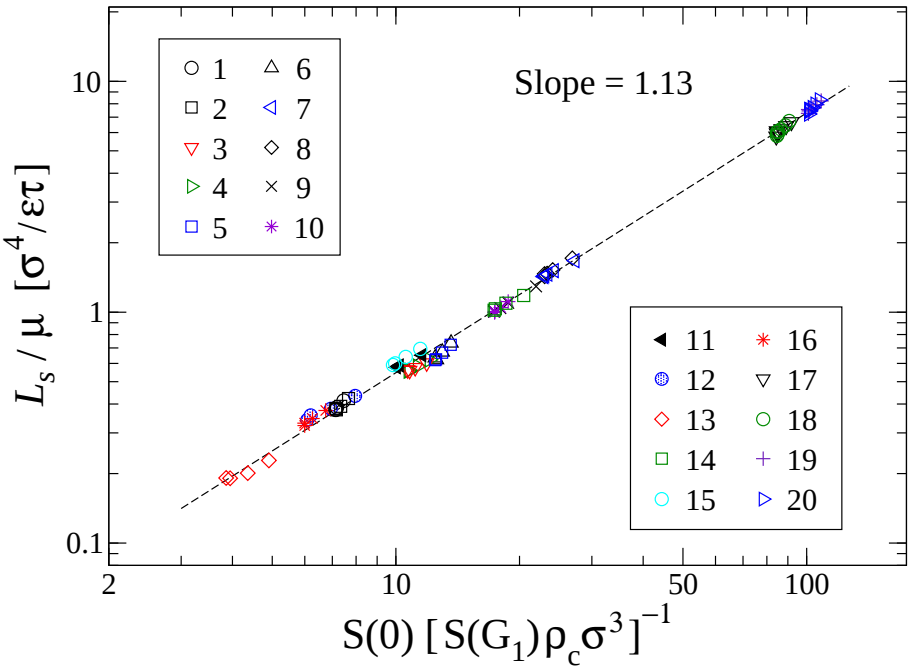

FIG. 16: (Color online) Log-log plot of the ratio L_s/μ (in units $\sigma^4/\varepsilon\tau$) as a function of the variable $S(0)/\left[S(\mathbf{G}_1)\,\rho_c\right]$ computed in the first fluid layer at low shear rates. The system parameters are listed in Table I. The dashed line $y = 0.041\,x^{1.13}$ is the best fit to the data. Adapted from [51].

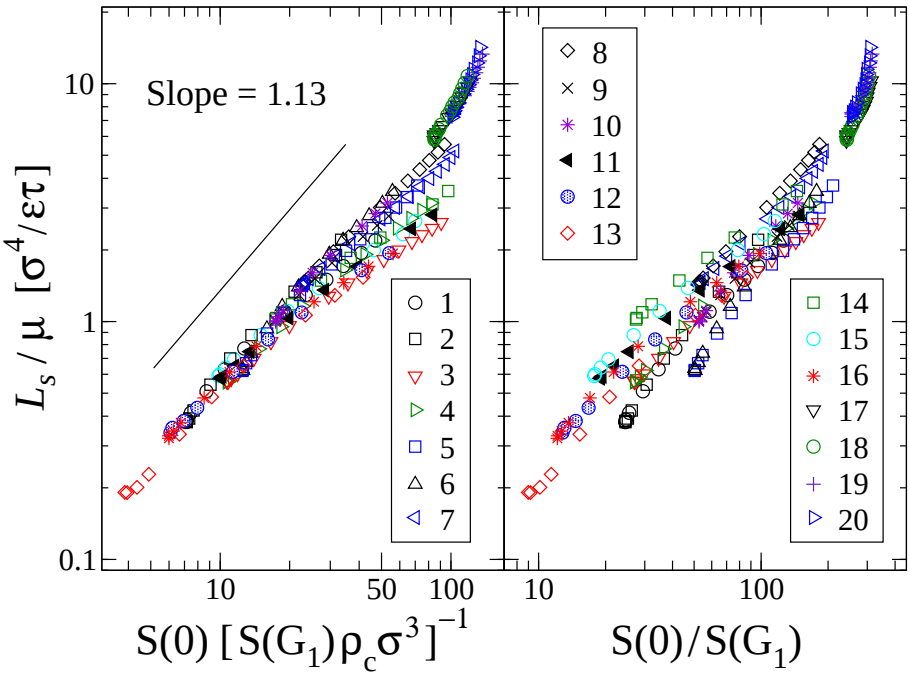

FIG. 17: (Color online) Log-log plot of the ratio L_s/μ (in units of $\sigma^4/\varepsilon\tau$) as a function of variables (a) $S(0)/\left[S(\mathbf{G}_1)\,\rho_c\right]$ and (b) $S(0)/S(\mathbf{G}_1)$ computed in the first fluid layer at all shear rates examined. The system parameters are given in Table I. The same data as in Fig. 7. The black line with a slope 1.13 is shown for reference. Reprinted from [51].

Tables

TABLE I: The fluid monomer density $\rho = N_f/A_{xy}(h-\sigma)$, number of monomers per chain N, distance between the wall lattice planes in contact with fluid h, wall area in the xy plane, fluid pressure at equilibrium (i.e., $U = 0$), wall density ρ_w, lattice type, Miller indices for the xy plane, lattice orientation along the shear flow direction ($\hat{x}$ direction), the $\hat{x}$ and $\hat{y}$ components of the first reciprocal lattice vector $\mathbf{G}_1(k_x, k_y)$, wall-fluid interaction energy, and the spring stiffness coefficient for thermal walls. Adapted from [51].

No.	$\rho\sigma^3$	N	h/σ	A_{xy}/σ^2	$P/\varepsilon\sigma^{-3}$	$\rho_w\sigma^3$	Type	(ijk)	$\hat{x}$	$(k_x\sigma, k_y\sigma)$	$\varepsilon_{\text{wf}}/\varepsilon$	$\kappa/\varepsilon\sigma^{-2}$
1	0.91	20	22.02	502.28	1.0	1.40	fcc	(111)	$[11\bar{2}]$	(7.23, 0)	0.9	Fixed
2	0.91	20	22.02	502.28	1.0	1.40	fcc	(111)	$[1\bar{1}0]$	(6.26, 3.62)	0.9	Fixed
3	0.88	20	19.46	589.79	0.5	1.10	fcc	(111)	$[11\bar{2}]$	(6.67, 0)	0.8	1200
4	0.88	20	19.46	589.79	0.5	1.10	fcc	(111)	$[1\bar{1}0]$	(5.78, 3.34)	0.8	1200
5	0.89	20	26.44	424.73	0.5	1.80	fcc	(111)	$[11\bar{2}]$	(7.86, 0)	1.0	Fixed
6	0.89	20	26.44	424.73	0.5	1.80	fcc	(111)	$[1\bar{1}0]$	(6.81, 3.93)	1.0	Fixed
7	0.83	10	23.93	502.28	0.0	1.40	fcc	(111)	$[11\bar{2}]$	(7.23, 0)	0.7	1200
8	0.83	10	23.93	502.28	0.0	1.40	fcc	(111)	$[1\bar{1}0]$	(6.26, 3.62)	0.7	1200
9	0.88	20	24.72	459.42	0.5	1.60	fcc	(111)	$[11\bar{2}]$	(7.56, 0)	0.8	1200
10	0.88	20	24.72	459.42	0.5	1.60	fcc	(111)	$[1\bar{1}0]$	(6.55, 3.78)	0.8	1200
11	0.89	20	19.12	595.87	0.5	1.90	bcc	(001)	[100]	(6.18, 0)	0.4	Fixed
12	0.89	20	19.12	595.87	0.5	1.90	bcc	(001)	[100]	(6.18, 0)	0.5	Fixed
13	0.89	20	19.12	595.87	0.5	1.90	bcc	(001)	[100]	(6.18, 0)	0.6	Fixed
14	0.85	10	19.98	595.87	0.5	1.90	bcc	(001)	[100]	(6.18, 0)	0.4	1200
15	0.85	10	19.98	595.87	0.5	1.90	bcc	(001)	[100]	(6.18, 0)	0.5	1200
16	0.85	10	19.98	595.87	0.5	1.90	bcc	(001)	[100]	(6.18, 0)	0.6	1200
17	0.81	1	34.86	350.61	2.36	2.40	fcc	(111)	$[11\bar{2}]$	(8.65, 0)	0.4	Fixed
18	0.81	1	34.86	350.61	2.36	2.40	fcc	(111)	$[1\bar{1}0]$	(7.49, 4.33)	0.4	Fixed
19	0.81	1	34.86	350.61	2.36	2.40	fcc	(111)	$[11\bar{2}]$	(8.65, 0)	0.3	Fixed
20	0.81	1	34.86	350.61	2.36	2.40	fcc	(111)	$[1\bar{1}0]$	(7.49, 4.33)	0.3	Fixed